these units are linked only by corner sharing of octahedra, whilst in $W_{18}O_{49}$ edge sharing also occurs. It is this feature that reduces the oxygen-to-metal ratio in this latter phase compared to $W_{17}O_{47}$. A comparison with the oxide $W_{24}O_{68}$ is also marked and the connectivity within a group of 24 polyhedra is the same in both structures.

It is interesting to note that the molybdenum oxide of equivalent composition, $Mo_{17}O_{47}$, has the somewhat different, but related structure (Kihlborg, 1960, 1963) shown in Fig. 7(*d*). Here the MoO_7 pentagonal bipyramids are joined together by edge sharing, resembling the arrangement in $W_{18}O_{49}$. In the Mo oxide, however, the hexagonal tunnels are blocked by O atoms. By comparison, it is apparent that $Mo_{17}O_{47}$ is more closely related structurally to $W_{18}O_{49}$ than to its compositional equivalent $W_{17}O_{47}$.

The present study has elucidated, by high-resolution electron microscopy, the likely structure of a new tungsten oxide. It forms in the presence of Sb and in this respect can be compared with the pseudo-binary oxide W_5O_{14}. It seems possible, therefore, that these materials form part of a series of related phases which are only stable over narrow ranges of temperature and composition in the presence of one or more ternary metals. A comprehensive search for other new phases would be of interest. Such a study, as well as a refinement of the structure of the phase described in this paper, will be reported in future communications.

MMD is indebted to ICI New Science Group, Runcorn, Cheshire, for financial support.

References

EKSTRÖM, T. & TILLEY, R. J. D. (1976). *J. Solid State Chem.* **19**, 125–133.
KIHLBORG, L. (1960). *Acta Chem. Scand.* **14**, 1612–1622.
KIHLBORG, L. (1963). *Acta Chem. Scand.* **17**, 1485–1487.
MAGNÉLI, A. (1949). *Ark. Kemi*, **1**, 223–230.
NORD, A. G. (1963). Dissertation, Univ. of Stockholm, Sweden.
PICKERING, R. & TILLEY, R. J. D. (1976). *J. Solid State Chem.* **16**, 247–255.
SAHLE, W. & SUNDBERG, M. (1980). *Chem. Scr.* **16**, 163–168.
SKARNULIS, A. J. (1976). PhD Thesis, Arizona State Univ., USA.
SUNDBERG, M. (1978). *Chem. Scr.* **14**, 161–166.
SUNDBERG, M. & LUNDBERG, M. (1987). *Acta Cryst.* B**43**, 429–434.
WERNER, P. E. (1969). *Ark. Kemi*, **31**, 513–516.
YVON, K., JEITSCHKO, W. & PARTHÉ, E. (1977). *J. Appl. Cryst.* **10**, 73–74.

Acta Cryst. (1988). B**44**, 480–486

Structure of Al_mFe

BY PER SKJERPE

Department of Physics, University of Oslo, PO Box 1048, *Blindern* 0316, *Oslo* 3, *Norway*

(*Received* 27 *October* 1987; *accepted* 28 *April* 1988)

Abstract

The metastable phase Al_mFe ($m = 4{\cdot}0$–$4{\cdot}4$, body-centred tetragonal, $a = 8{\cdot}84$, $c = 21{\cdot}6$ Å) has been examined by transmission electron microscopy and high-resolution electron microscopy (HREM). Crystals, 1–10 μm in size, were extracted from a cast Al–0·25wt%Fe–0·13wt%Si alloy of commercial purity. By the use of electron diffraction patterns, a possible structure model for Al_mFe was set up, assuming space group *I*4/*mmm*. The model was in qualitative agreement with diffraction patterns as well as HREM micrographs, recorded in ⟨100⟩ and ⟨110⟩. Streaks along *hh*0 in the diffraction patterns were ascribed to faults on (110).

1. Introduction

Iron and silicon are always present in commercial aluminium alloys and primary particles of Al–Fe and Al–Fe–Si are usually precipitated during casting. The particle types appearing depend on alloy composition (Fe/Si ratio) and the cooling rate during solidification. Low cooling rates favour formation of equilibrium phases, higher cooling rates cause metastable Al–Fe(–Si) phases to be formed (Westengen, 1982).

The crystal structures of most equilibrium Al–Fe–Si phases have been determined (Black, 1955*a*,*b*; Walford, 1965; Cooper, 1967; Cooper & Robinson, 1966; Corby & Black, 1977). On the other hand, the structures of most metastable Al–Fe–Si phases are not known, except approximate lattice parameters and chemical compositions. X-ray diffraction studies of these particles encounter difficulties; the crystals are a few micrometres in size and usually a mixture of phases will be contained in the ingot. Thus transmission electron microscopy (TEM) is essential for analyzing the structure of these particles.

During a TEM study of particles in a cast Al–Fe–Si alloy (Skjerpe, 1987), one of the metastable phases

0108-7681/88/050480-07$03.00

observed was Al_mFe. This particle type is of interest for material applications, since its presence may degrade the surface quality of aluminium. Its crystal structure has not been determined, and therefore it was decided to carry out a more detailed TEM study of this phase. The current paper presents the results, and a possible structure, derived by using TEM techniques, is described.

2. Previous work on Al_mFe

The unit cell of Al_mFe is body-centred tetragonal with $a = 8{\cdot}84$ and $c = 21{\cdot}6$ Å (Miki, Kosuge & Nagahama, 1975). The value of m has been measured by energy-dispersive specroscopy to be 4·4 (Westengen, 1982), 4·2 (Skjerpe, 1987) and 4·0 (Porter & Westengen, 1981).

The probable space group is *I*4/*mmm*, as found by convergent-beam electron diffraction (Skjerpe, Gjønnes & Langsrud, 1987). The symmetry was consistent with *I*4/*mmm* or *I*4*mm*, which are centro- and noncentrosymmetrical respectively. The structure had a centre of symmetry, indicating the space group *I*4/*mmm*. On the other hand, attempts to observe the mirror 4/*m* failed, but this was ascribed to the presence of crystal defects.

Only a schematic X-ray diffraction pattern has been published (Asami, Tanaka & Hideno, 1978), indicating a few low-order reflections.

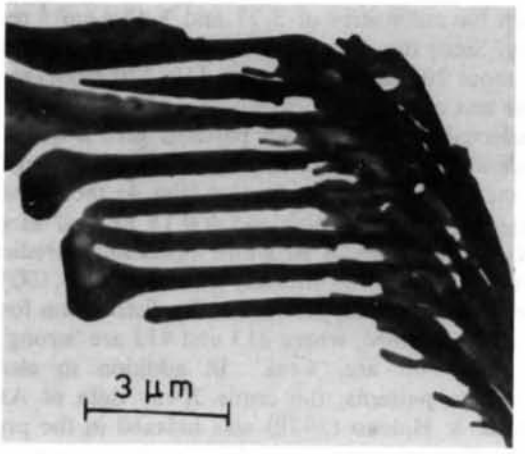

Fig. 1. Typical morphology of Al_mFe. Extracted crystal on holey carbon film.

3. Experimental

Crystals were obtained from a direct-chill cast Al–0·25wt%Fe–0·13wt%Si alloy of commercial purity. Samples were taken at 25 mm from the ingot surface, where the local cooling rate had been high ($6\,K\,s^{-1}$) and produced considerable amounts of Al_mFe. Samples were also taken at 100 mm from the surface, where some Al_mFe had been formed, in spite of the low cooling rate ($1\,K\,s^{-1}$). A survey of the phases has been published elsewhere (Skjerpe, 1987).

Extracted crystals, suitable for TEM, were prepared by dissolving the aluminium phase in butanol, followed by filtering and dispersing the extracted particles on holey carbon films. The extraction procedure is described elsewhere (Simensen, Fartum & Andersen, 1984; Strid & Simensen, 1986).

The crystals were examined at 200 kV in a JEOL 2000FX microscope, equipped with a double-tilt goniometer. The spherical aberration constant was 2·3 mm, giving 0·28 nm resolution for high-resolution electron microscopy (HREM).

4. Crystal morphology

The morphology is complex (Fig. 1) and the particles resemble 'skeletons' with protruding fingers. The morphology is similar to a eutectic constituent, suggesting that Al_mFe is formed by a metastable eutectic

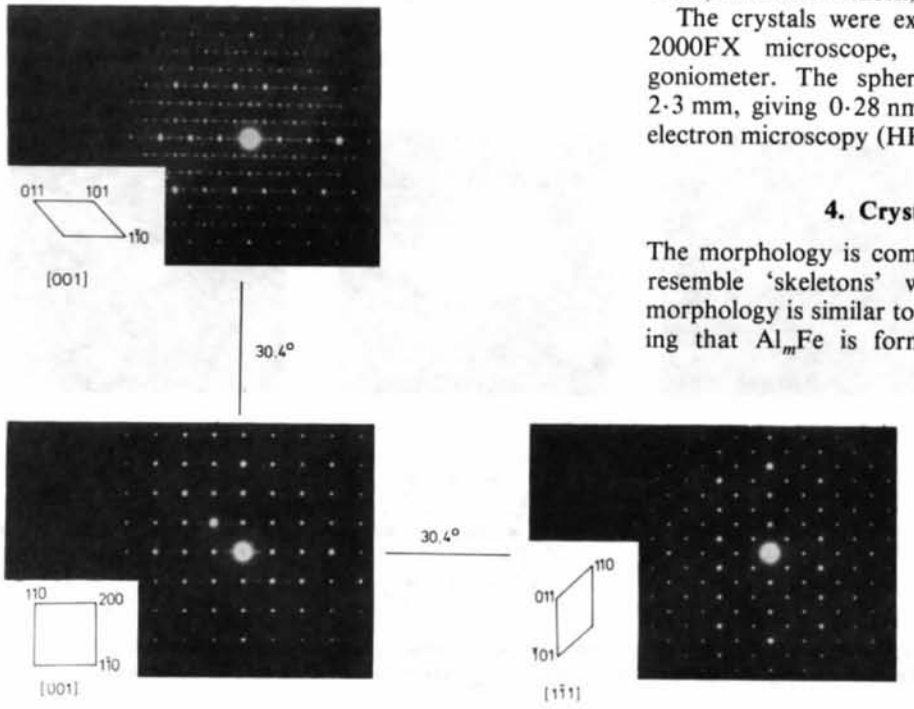

Fig. 2. Double-axis-tilt series of Al_mFe, verifying the tetragonal lattice. Note the different strength of super reflections in the two ⟨111⟩ projections.

reaction. The particles were single crystals and commonly up to 10 μm in size. No difference between protruding fingers and the main part of the particle was apparent in the diffraction patterns.

5. Bravais lattice

In order to verify the body-centred tetragonal lattice, a tilt series was carried out, using a crystal having its c axis along the electron beam (Fig. 2). By tilting around either $hh0$ row, two $\langle 111 \rangle$ patterns were observed in good agreement with the lattice parameters. Thus the tetragonal lattice was verified. No attempts were made to measure more accurate lattice parameters.

6. Streaks and super reflections

Streaks and super reflections were observed in most diffraction patterns. In order to characterize the streaks, tilt series were carried out. The experiments showed that the streaks could be described simply: each point hkl is traversed by two orthogonal streaks, which are parallel to $\langle 110 \rangle$ directions. This is illustrated in Fig. 3, where patterns have been drawn by marking intersections between streaks and various planar sections in reciprocal space. As shown in Fig. 3, the geometry of the streaks is described quite well.

The $\langle 110 \rangle$ streaks are not fully continuous lines, intensity modulations cause some super spots to appear stronger and others weaker in Fig. 3. For the particular crystal in Fig. 2, the 110 streaks are more prominent than $1\bar{1}0$ streaks. Therefore the two $\langle 111 \rangle$ projections appear different with respect to super reflections.

Crystals formed at 25 mm distance (high cooling rate) generally displayed more pronounced streaking than crystals at 100 mm distance (low cooling rate). This indicates that the streaks are caused by (110) faults, which mainly occur in crystals formed at higher cooling rates.

7. A possible structure for Al_mFe

A possible model structure, derived from TEM results, is presented in this section. It should be noted that no isostructural phase could be found in the literature and no relation to other Al–Fe(–Si) phases of known crystal structure is apparent.

The density is not known, but an estimate was obtained by assuming a density between those of $Al_{13}Fe_4$ (Black, 1955*a*) and Al_6Fe (Walford, 1965), which have densities of 3·77 and 3·45 g cm^{-3} respectively. Since the m value is between 4·0 and 4·4, there are about 20–22 Fe atoms and 110–120 atoms in total in the unit cell.

Selected-area diffraction patterns give a qualitative indication of which diffraction spots are strong. For instance, in the $\langle 100 \rangle$ projection (Fig. 4), there is strong scattering into 307, 600 and 0,0,14 as well as other spots, such as 006. A structure model must predict the major features of the intensity distribution in $\langle 100 \rangle$ and other projections. In particular, the distribution for $hk3$ must be explained, where 213 and 413 are 'strong' and 103 and 303 are 'weak'. In addition to electron diffraction patterns, the crude X-ray data of Asami, Tanaka & Hideno (1978) was indexed in the present study. The results are given in Table 1, and support the qualitative intensity distribution observed in electron diffraction.

If 307, 330, 600 and 0,0,14 are assumed 'fundamental' (most atoms scatter in phase), then an average, nearly b.c.c. subunit of dimensions $a/3$ (0·295 nm) and

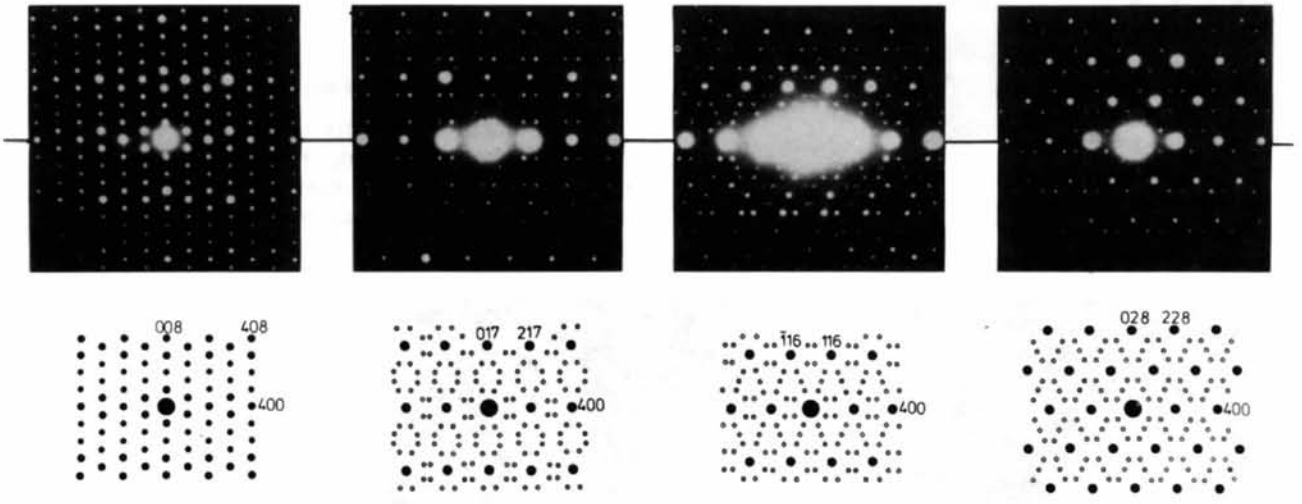

Fig. 3. Tilt series for examination of streaking effects. The diffraction patterns have been compared with the geometrical model of the streaks (see text). The positions of super reflections are in good agreement with the model. However, there are intensity differences among super reflections.

$c/7$ (0·309 nm) is indicated. Such units are accommodated in the unit cell by placing atoms at heights $z = 0$ and z near $\frac{1}{7}$ in (0,0,z), (x,0,z) and (x,x,z), where x is near $\frac{1}{3}$, and furthermore at heights z near $\frac{1}{14}$ and $\frac{3}{14}$ in (x,x,z), ($\frac{1}{2}$,x,z) and ($\frac{1}{2}$,$\frac{1}{2}$,z) where x is near $\frac{1}{6}$. This ideal average framework has 126 atoms in the tetragonal cell and produces the fundamental reflections mentioned above.

To arrive at a model from this ideal framework, it is required: (1) to introduce 'vacant' positions (8–16 'vacancies' are needed), (2) to locate the Fe atoms (20–22 Fe atoms), (3) to perform displacements from the ideal positions.

'Vacancies' and Fe atoms represent deviations from the ideal stacking and their location determines the intensities of reflections other than the fundamental reflections mentioned above.

The difference between Fe and Al electron-scattering factors is not very large for low-order reflections. This has been illustrated in Fig. 5, where the scattering amplitudes are plotted. Accordingly, low-order reflections are sensitive mainly to the location of 'vacancies' and not to Fe atoms. On the other hand, higher-order reflections are obviously sensitive to Fe atoms.

Table 1. *Strong X-ray lines from* Al_mFe

The list was set up by indexing the X-ray pattern given by Asami, Tanaka & Hideno (1978).

d(nm)	hkl	d(nm)	hkl
0·624	110	0·221	400
0·440	200	0·215	?
0·406	114	0·214	307
0·346	213	0·208	330
0·242	217	0·205	413

From experiments, 213 and 413 are 'strong' and 103 and 303 'weak'. This distribution is not easily obtainable in $I4/mmm$, if reasonable interatomic distances are requested. However, one distribution of Fe and 'vacancies' was found about acceptable: the 'vacancies' were put in the 16-fold position ($\frac{1}{3}$,0,$\frac{1}{7}$), since other arrangements gave no appreciable intensity to the low-order 213 reflection. The Fe atoms were put in (0,0,$\frac{1}{7}$) and ($\frac{1}{3}$,$\frac{1}{3}$,$\frac{1}{7}$), since other arrangements gave no appreciable intensity to the high-order reflection 413. This arrangement has 110 (20 Fe and 90 Al) atoms in the unit cell, $m = 4{\cdot}5$ and a density 3·49 g cm^{-3}.

In order to obtain a qualitatively correct distribution for the 001 row, the Fe z coordinates were slightly decreased. This adjustment tends to equalize the distance between Fe layers in the z direction.

In Fig. 6 the resulting structure is drawn in ⟨010⟩ projection. The structure has Fe layers parallel to (001), separated by two and three Al layers. Alternatively, there are nearly equidistant Fe layers separated by 2·5 Al layers on average.

The kinematical electron intensities (structure factors squared) gave qualitative agreement with the diffraction patterns. The calculated electron structure factors are listed in Table 2. It should be noted that a fully satisfying distribution for $hk3$ reflections could not

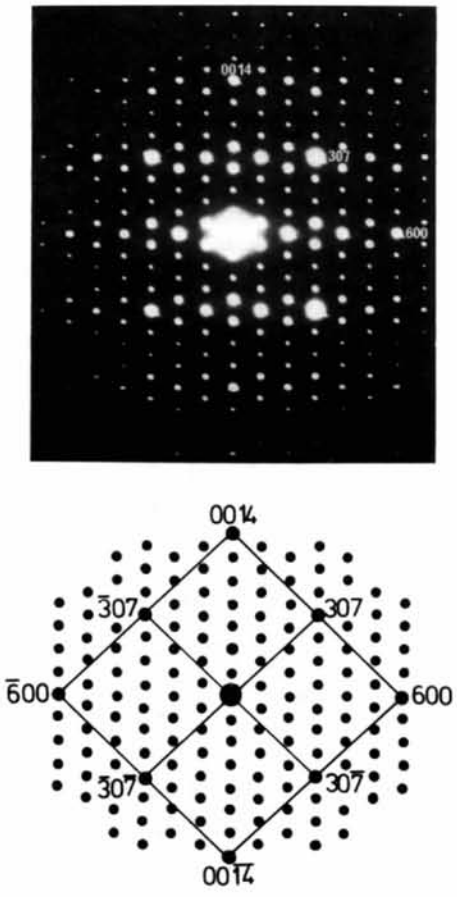

Fig. 4. Typical diffraction pattern in ⟨100⟩ projection. The strong reflections 600, 307 and 0,0,14 were assumed to be associated with a nearly b.c.c. unit of dimensions $a/3$, $a/3$, $c/7$.

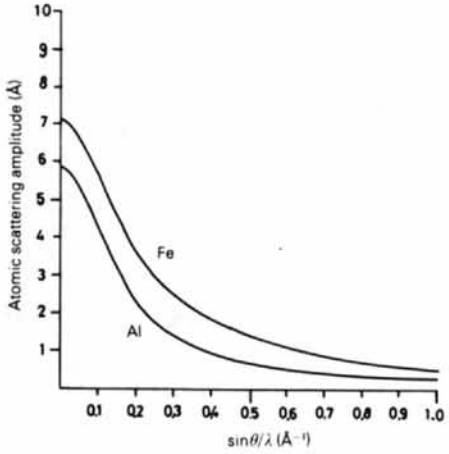

Fig. 5. Comparison between electron-scattering amplitudes for Al and Fe.

be obtained. Thus, the main discrepancy with experiments is the value of the 103 reflections in Table 2, which is relatively too high.

8. High-resolution electron microscopy

In order to check the model, HREM was carried out. In Fig. 7 a simulated through-focus series in ⟨100⟩ is shown. The weak-phase object approximation has been assumed.

In Fig. 8 a typical ⟨100⟩ HREM image is shown. Near the thin crystal edge, the calculated and experimental images agree quite well, indicating that the main

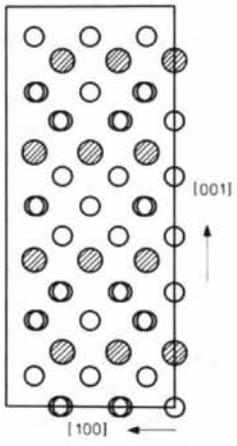

Fig. 6. Possible structure of Al_mFe, viewed in ⟨100⟩ projection. Layers of Fe atoms on (001) are separated by two or three layers of Al atoms.

Table 2. *Calculated structure factors for electrons* (V) *from model structure of* Al_mFe

Only structure factors larger than 0·7 V are given.

h	k	l	d(nm)	V_{hkl}
1	1	0	0·629	1·0
1	0	3	0·559	0·8
2	0	0	0·445	−1·1
1	1	4	0·410	−1·3
2	1	1	0·391	0·7
0	0	6	0·360	−1·3
2	1	3	0·348	−0·8
2	2	0	0·315	1·4
2	1	7	0·244	0·8
0	0	10	0·216	1·1
3	0	7	0·213	6·1
3	3	0	0·210	6·0
4	1	3	0·207	−0·8

distribution of scattering material within the projected unit cell is in accord with the model, *i.e.* signs and relative magnitudes of low-order Fourier coefficients are in agreement. The main discrepancy between the experimental and calculated images is caused by the too strong 103 structure factor (see previous comment on $hk3$ reflections).

HREM images were also recorded in ⟨110⟩. The typical diffraction pattern from this projection is shown in Fig. 9. The super reflections along $hh0$ are quite prominent in this zone and have been indicated in the figure. The calculated HREM images (weak-phase object approximation) are shown in Fig. 10.

A ⟨110⟩ HREM image is shown in Fig. 11. The modulations on (110), corresponding to the super reflections, are easily seen in thicker regions. Most HREM images in this projection had lower symmetry

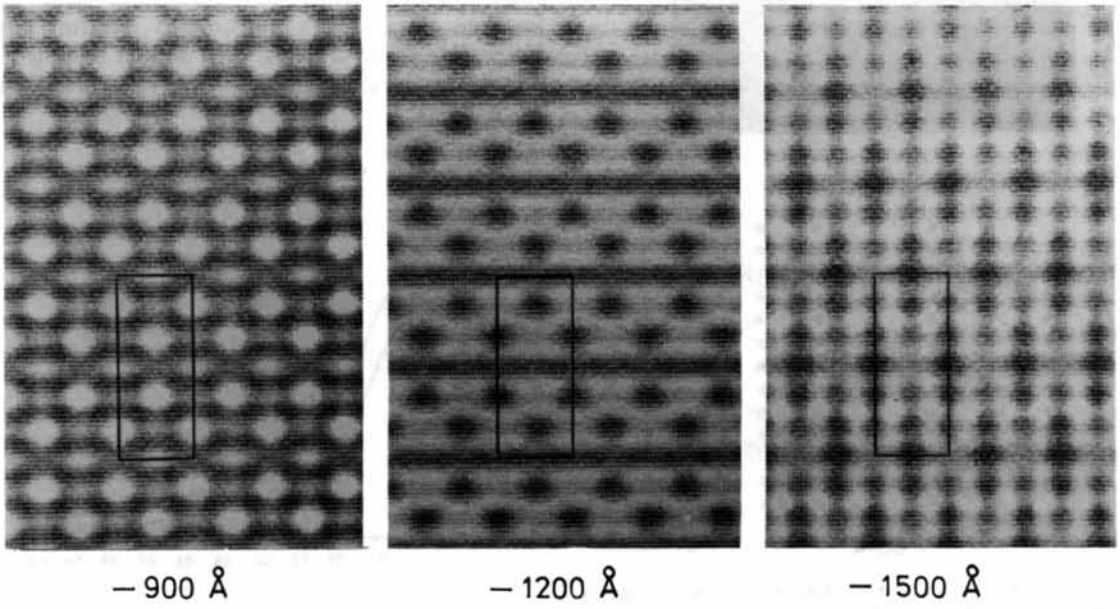

Fig. 7. Simulated ⟨100⟩ HREM images. Extended Scherzer focus is about −90 nm. The weak-phase object approximation has been assumed. The tetragonal unit cell has been indicated.

than assumed, indicating that small crystal tilts off the zone axis are important. Near the thin edges of the crystals, regions with 'correct' symmetry could be found (Fig. 12) and matched quite well with calculated images. The defocus in Fig. 12 is −90 nm, which is near the extended Scherzer focus. The matching is approximate, but the signs of the Fourier coefficients are in overall agreement.

9. Discussion

A possible model for Al_mFe was derived by assuming: (1) the space group is $I4/mmm$; (2) the density is

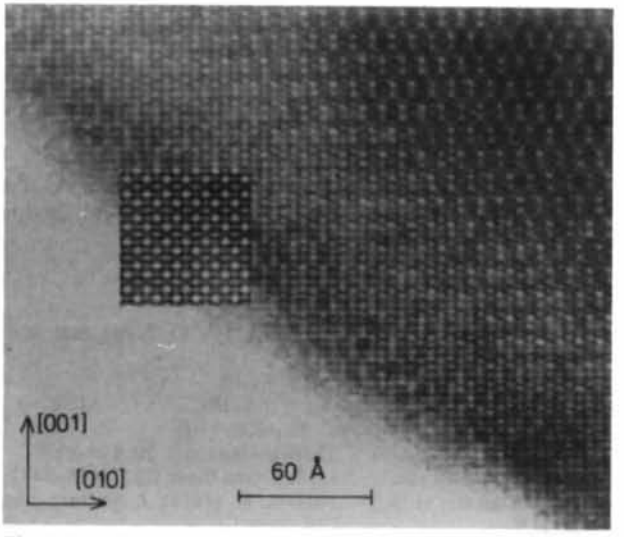

Fig. 8. Experimental HREM image in ⟨100⟩ projection. Reasonable image matching was obtained near the thin edge. Simulated image (defocus −90 nm) inserted.

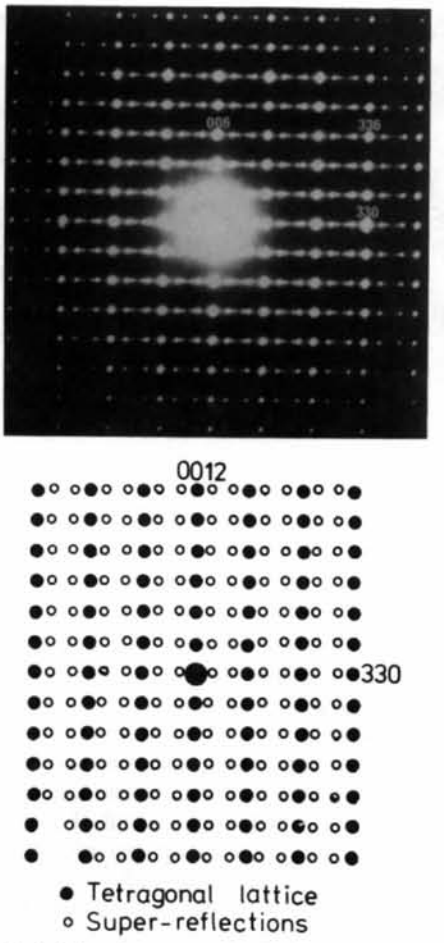

Fig. 9. Typical diffraction pattern in ⟨110⟩. Super reflections are quite prominent in this projection.

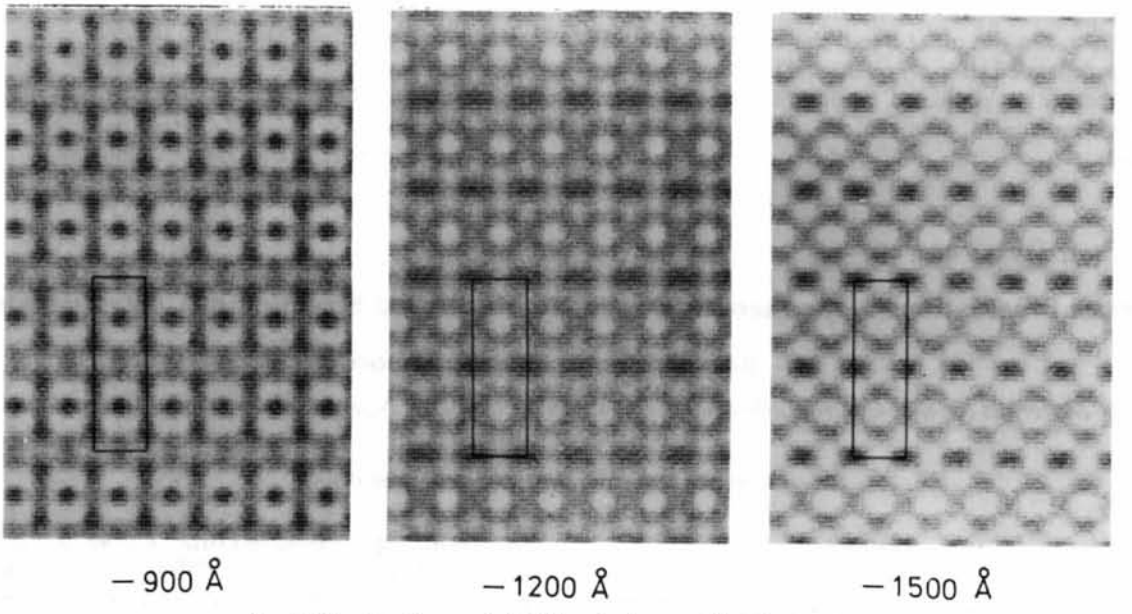

Fig. 10. Simulated images in ⟨110⟩ projection, see Fig. 7 for details.

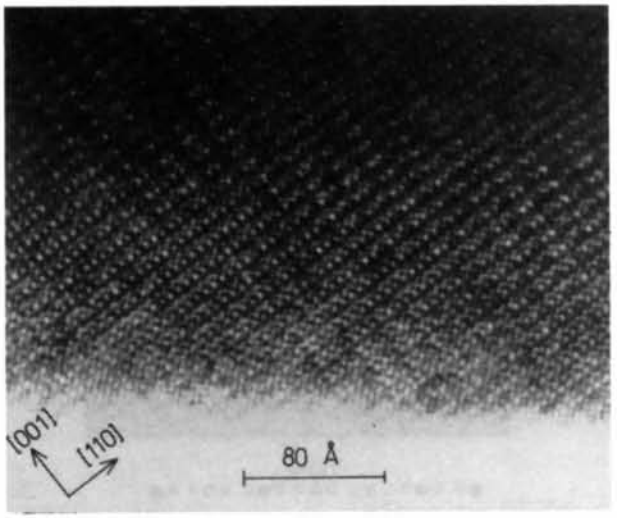

Fig. 11. Typical HREM image in ⟨110⟩. The modulations on (110) are easily seen in the thicker part of the crystal.

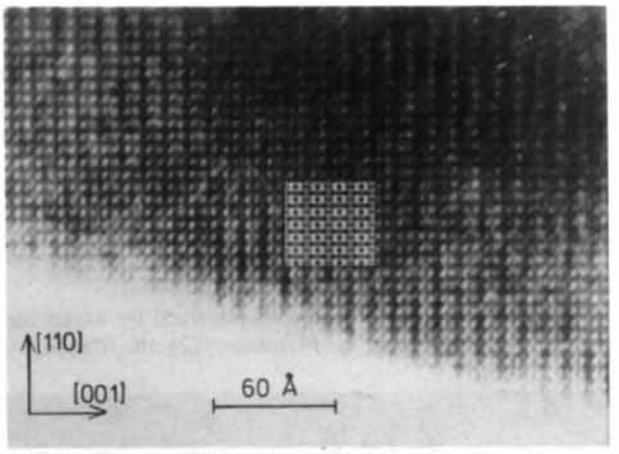

Fig. 12. Comparison between experimental and simulated image in ⟨110⟩. Defocus −90 nm. Reasonable image matching was obtained.

compatible with Al–Fe phases in the same composition range; (3) the m value is ~4·0–4·4; (4) the strongest diffraction spots are fundamental, *i.e.* most atoms scatter in phase.

From these assumptions, a framework of 126 atoms in the unit cell was set up, which produced the strongest diffraction spots. 'Vacancies' and Fe atoms were distributed in the framework by trial and error to obtain the correct 'strong' and 'weak' reflections for the other diffraction spots. The model gave qualitative, but not fully satisfying, agreement with diffraction patterns.

The model could explain the experimental HREM images, in the ⟨100⟩ as well as the ⟨110⟩ projection. This suggests that the main features of the model may be correct. On the other hand, the contrast of HREM images depended strongly on crystal thickness, questioning whether a projected structure interpretation of HREM images is applicable, even for the thinnest crystals.

In order to obtain a better structure model for Al_mFe, more experimental data, such as HREM at higher resolution, are needed.

References

Asami, S., Tanaka, T. & Hideno, A. (1978). *J. Jpn Inst. Met.* **28**(7), 321–327.

Black, P. J. (1955*a*). *Acta Cryst.* **8**, 43–48.

Black, P. J. (1955*b*). *Acta Cryst.* **8**, 175–181.

Cooper, M. (1967). *Acta Cryst.* **23**, 1106–1107.

Cooper, M. & Robinson, K. (1966). *Acta Cryst.* **20**, 614–617.

Corby, R. N. & Black, P. J. (1977). *Acta Cryst.* B**33**, 3468–3473.

Miki, I., Kosuge, H. & Nagahama, K. (1975). *J. Jpn Inst. Met.* **25**(1), 1–9.

Porter, D. A. & Westengen, H. (1981). *Quantitative Microanalysis with High Spatial Resolution*, pp. 94–100. London: The Metals Society.

Simensen, C. J., Fartum, P. & Andersen, A. (1984). *Fresenius Z. Anal. Chem.* **319**, 286–292.

Skjerpe, P. (1987). *Metall. Trans.* **18**A, 189–200.

Skjerpe, P., Gjønnes, J. & Langsrud, Y. (1987). *Ultramicroscopy*, **22**, 239–250.

Strid, J. & Simensen, C. J. (1986). *Pract. Metall.* **23**, 485–492.

Walford, L. K. (1965). *Acta Cryst.* **18**, 287–291.

Westengen, H. (1982). *Z. Metallkd.* **73**(6), 360–368.

Acta Cryst. (1988). B**44**, 486–494

Valence Fluctuations in the Incommensurately Modulated Structure of Calaverite $AuTe_2$

By W. J. Schutte and J. L. de Boer

Materials Science Centre, Laboratory of Inorganic Chemistry, Nijenborgh 16, 9747 *AG Groningen, The Netherlands*

(*Received* 15 *December* 1987; *accepted* 6 *June* 1988)

Abstract

The incommensurately modulated structure of calaverite $Au_{1-p}Ag_pTe_2$ ($p < 0·15$) with modulation wavevector $\mathbf{q} = -0·4076\,(16)\mathbf{a}^* + 0·4479\,(6)\mathbf{c}^*$, has been determined by X-ray diffraction at room temperature and at 100 K (3012 and 3017 independent reflections, respectively). The symmetry of the struc-

0108-7681/88/050486-09$03.00